

**Dual mechanism of ion-(de)intercalation and iodine redox towards
advanced zinc battery**

Yongqiang Yang,^a Shan Guo,^a Yicai Pan,^a Bingan Lu,^b Shuquan Liang^{a,*} and Jiang Zhou^{a,*}

^a *School of Materials Science and Engineering, Hunan Provincial Key Laboratory of Electronic Packaging and Advanced Functional Materials, Central South University, Changsha 410083, China,*
E-mail: lsq@csu.edu.cn; zhou_jiang@csu.edu.cn.

^b *School of Physics and Electronics, Hunan University, Changsha 410082, China.*

Experimental section

Preparation of electrolyte

All the reagents mentioned were from Aladdin. Firstly, the base electrolytes were prepared by dissolving 3 M Zn(CF₃SO₃)₂ in an ethylene glycol/water (EG/H₂O) binary solvent, where the volume fraction of EG was controlled to be 0, 30, 60, 90, 100%, respectively. Then, 0.1 M ZnI₂ was added to the above series of solutions as the sole iodine source. All ingredients were placed in sealed bottles and stored overnight at 60 °C to become uniform and clear. For the convenience of description, these solutions are abbreviated according to the concentration (or ratio) of components. For example, a solution of 3 M Zn(CF₃SO₃)₂ and 0.1 M ZnI₂ in 90% EG/H₂O was labeled 3–01–90.

In addition, 3 M Zn(CF₃SO₃)₂ and 0.1 M ZnI₂ in H₂O was used as the representative of aqueous electrolyte for comparison. The effect of iodine content was characterized using series solutions with concentration gradient ZnI₂ which followed the labeling rules described above.

Preparation of ammonium vanadate (NH₄V₄O₁₀, NVO)

The NH₄V₄O₁₀ was prepared using a one-step hydrothermal method.¹ Firstly, 1.170 g of NH₄VO₃ was dissolved in deionized water at 80 °C to form a light-yellow solution. Next, 1.891 g of C₂H₂O₄·2H₂O solid powder was added to the solution under magnetic stirring until it turned black-green. The resulting solution was subsequently transferred to a 50 mL autoclave and maintained in an oven at 140°C for 48 h. After natural cooling to room temperature, the products were collected and washed several times with deionized water. Finally, the NH₄V₄O₁₀ powder was obtained by drying at 60°C for 12 h.

Preparation of electrode and fabrication of zinc-ion battery

Zinc foil without any modification was used as anode. The active substance on cathode was bi-component, including the NVO as Zn²⁺ (de)intercalation host and porous activated carbon (1800 m² g⁻¹ in specific area, 5–8 μm in particle size, PAC) with iodine adsorption. In practice, a uniform slurry consisting of NVO, PAC, Acetylene black and Polyvinylidene fluoride (PVDF) in a weight ratio of 4:4:1:1 in N-Methyl pyrrolidone (NMP) was coated on a stainless-steel disc (400 mesh in aperture, 12 mm in diameter, SS), and the disc was kept at 80 °C overnight in a vacuum oven. This bifunctional cathode was labeled as NVO–PAC.

Coin cell (CR 2016) was assembled by inserting glass microfiber filters (Whatman) soaked with electrolyte (60 μ L in additive amount) between the electrodes in an open atmosphere. Different types of cells (*e.g.*, Zn/Zn, Zn/Cu, Zn/SS, Zn/NVO–PAC, SS/SS) were selected for characterization under various situations.

Material characterizations

Fourier Transform Infrared (FT–IR) and UV–vis adsorption spectra of electrolyte were probed by Thermo Nicolet 6700 and Evolution 220 at room temperature, respectively. Dataphysics OCA–20 was responsible for the measurement of the contact angle. The crystallographic phases involved were determined by Rigaku D/max 2500 X–ray powder diffractometer with Cu K α –radiation ($\lambda = 0.15405$ nm). The morphology with corresponding energy dispersive spectrometer (EDS) elemental mappings was detected by TESCAN Mira3 scanning electron microscopy (SEM), and the Titan G2 60–300 in charge of transmission electron microscopy (TEM), high–resolution TEM (HRTEM), selected area electron diffraction (SAED) patterns. The evolution of elemental valance was reflected by X–ray photoelectron spectroscopy (XPS), which was recorded by ESCALAB 250 Xi.

Electrochemical measurements

The cyclic voltammetry (CV), liner sweep voltammetry (LSV), chronoamperometry (CA), liner polarization (or Tafel) curve and electrochemical impedance spectroscopy (EIS) from 100 kHz to 10 mHz were collected by CHI–660E. The galvanostatic charge–discharge (GCD) measurement was performed utilizing LAND CT2001A.

Electrochemical performance evaluation standard

Considering that this system stored energy through Zn²⁺ (de)intercalation and iodine redox with adsorption–desorption, of which the capacity contribution needs to be differentiated according to the reaction characteristics.

Zn²⁺ (de)intercalation: The (de)intercalation of Zn²⁺ triggers the valance state change of active elements (such as vanadium) in pristine NVO, further stimulating electron transfer. The capacity of

this process is more affected by the content of NVO in cathode, since there is always an excess of Zn^{2+} in electrolyte. This is the main reason for using specific capacity (unit: $mA\ h\ g^{-1}$) as capacity criterion in zinc-vanadium batteries. In this research, the content of NVO in obtained cathode is ~ 0.6 mg with the theoretical capacity of $490.2\ mA\ h\ g^{-1}$ for complete electron transfer. Notably, its quality serves as a criterion for current density during the GCD measurements to better compare with other cathodes in term of mass specific capacity based on the Zn^{2+} (de)intercalation.

Iodine redox with adsorption–desorption: It is noted that the iodine source in this system is added to the electrolyte in the form of I^- . Hence, I^-/I_2 conversion takes place at the interface between electrolyte and cathode, and PAC without iodine only assists electron transfer. The activity and depth of this reaction is directly affected by the area of cathode, not to mention that the additive amount of ZnI_2 in electrolyte is already limited. Hence, areal capacity (unit: $mA\ h\ cm^{-2}$) is used to describe the ability of iodine redox. In this research, the content of PAC in cathode is ~ 0.6 mg. Taking 3–01–90 electrolyte as an example, it can be calculated based on the component concentration and additive amount that the maximum capacity provided by complete single electron transfer of I^- is $0.43\ mA\ h$ ($0.38\ mA\ h\ cm^{-2}$ in areal capacity).

Molecular dynamics simulations

The molecular dynamics (MD) simulations were conducted in LAMMPS software. In the model of 3–01–90, 15 zinc ions, 1 iodide ions (I^-), 30 trifluoromethanesulfonate ions ($CF_3SO_3^-$) and 80 ethylene glycols, 30 water molecules were added. In the model of 3–01–00, 15 zinc ions, 1 iodide ions (I^-), 30 trifluoromethanesulfonate ions ($CF_3SO_3^-$) and 277 water molecules were added. Each system was equilibrated under the constant pressure–constant temperature (NPT) ensemble at constant pressure of 1 atm and temperature of 300 K by using 0.1 fs time step for 200 ps. Then, the canonical ensemble (NVT) condition was employed at 300 K by using 0.01 fs time step for 20 ps.

The radial distribution functions (RDFs) which reflected the probability of the distance between the atoms were calculated using the VMD analysis tool.

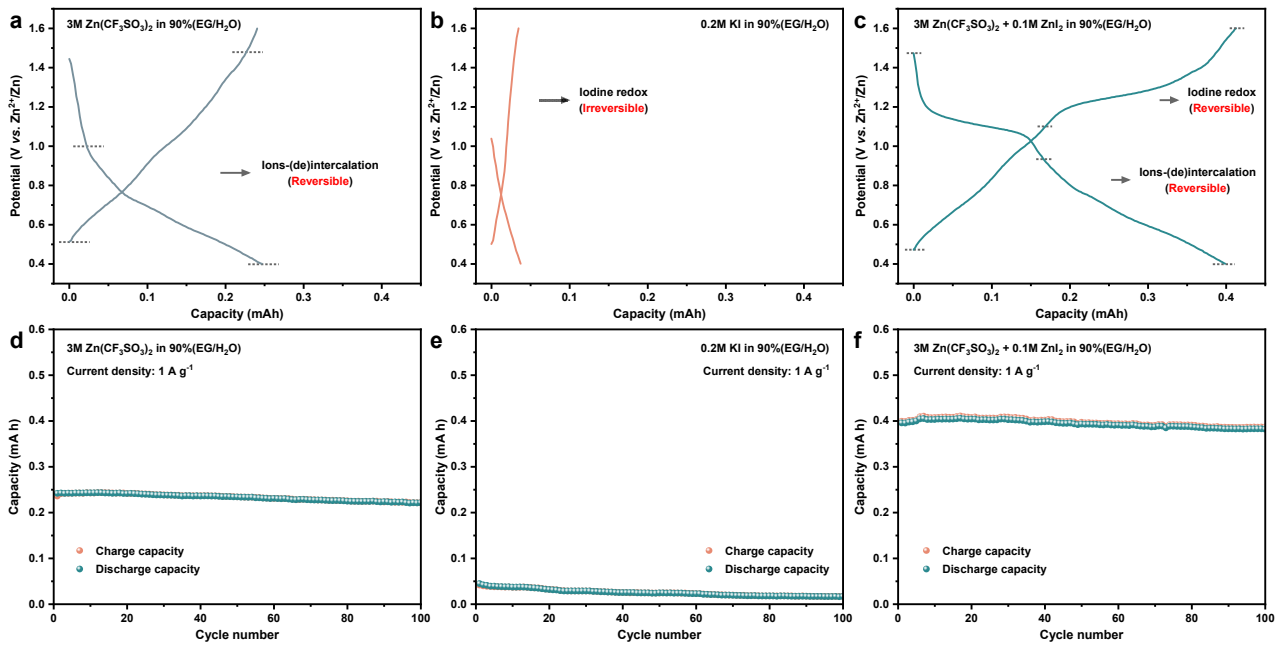


Figure S1. (a–c) GCD curves and (d–f) cycling performances of Zn/NVO–PAC cells with different ions–source electrolytes.

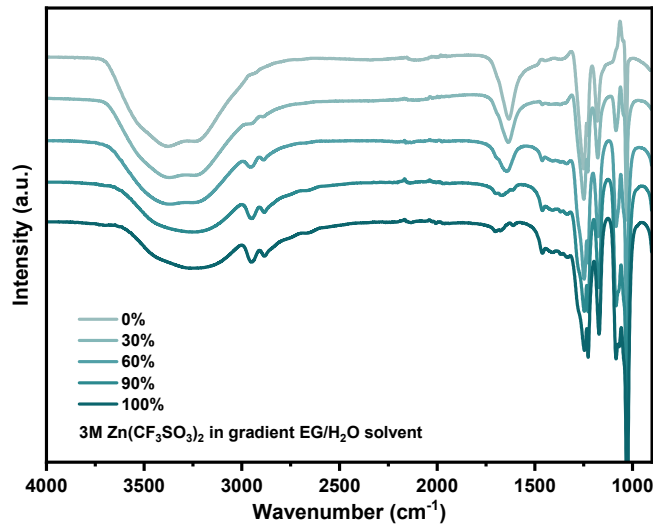


Figure S2. FT–IR spectra of 3 M $\text{Zn}(\text{CF}_3\text{SO}_3)_2$ in gradient EG/H₂O solvent.

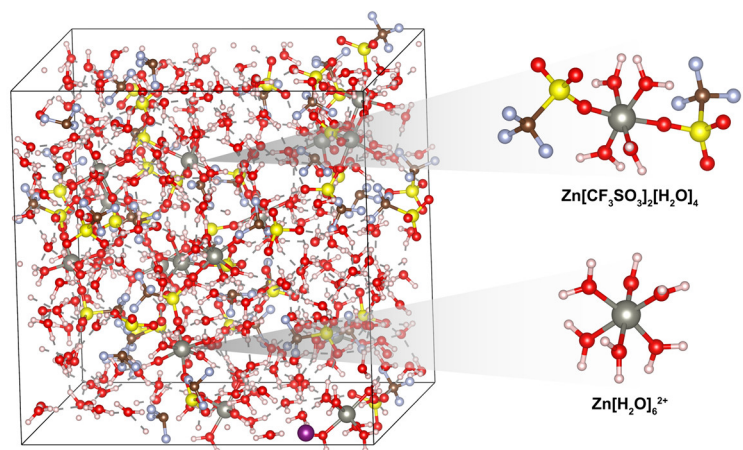


Figure S3. 3D snapshot obtained by the MD simulations of 3–01–00.

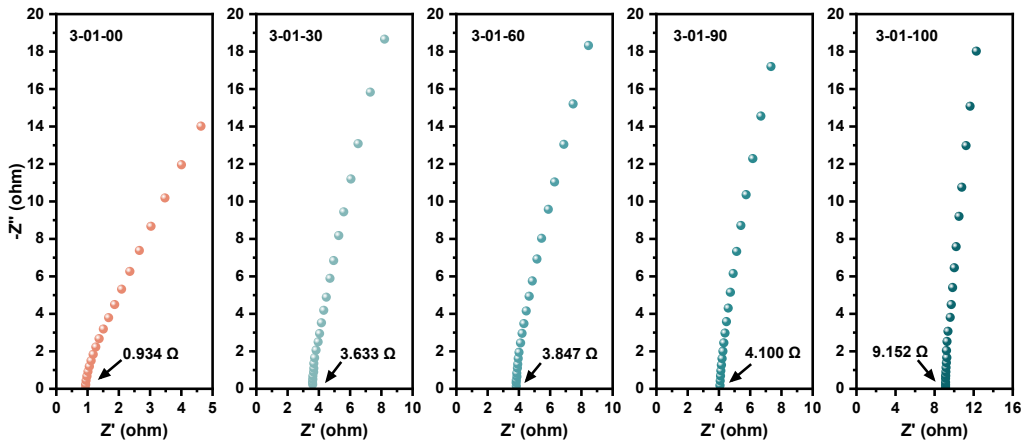


Figure S4. EIS spectra of SS/SS cells used electrolytes with gradient EG/H₂O solvent containing 3 M Zn(CF₃SO₃)₂ and 0.1 M ZnI₂, respectively.

The ionic conductivity (σ) of electrolytes was measured using the SS/SS cells (CR 2025), which was calculated as follow:

$$\sigma = \frac{l}{RA}$$

in which l , A and R represent the thickness (0.043 cm), covered area (1.96 cm⁻²) of electrolyte and bulk resistance (Ω).

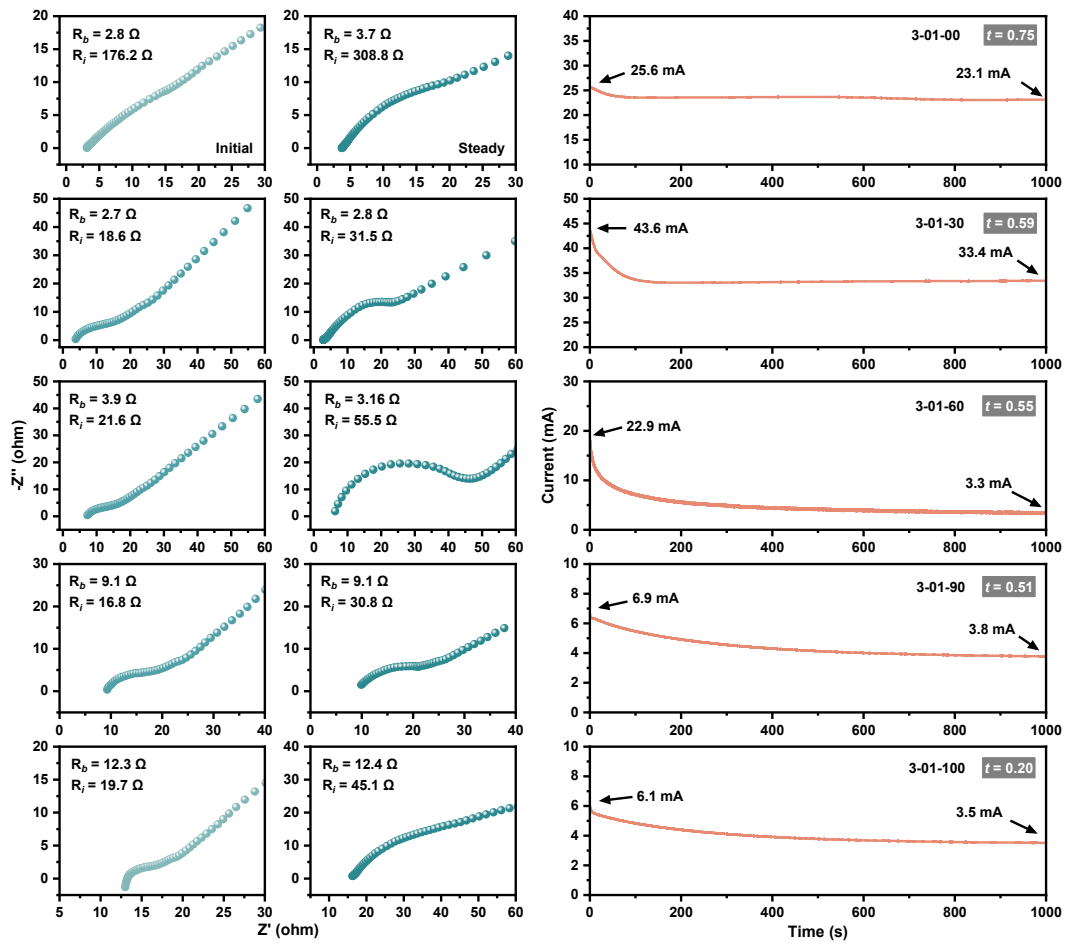


Figure S5. CA curves with a polarization voltage of 100 mV and represented EIS spectra before and after the polarization in Zn/Zn cells used electrolytes with gradient EG/H₂O solvent containing 3 M Zn(CF₃SO₃)₂ and 0.1 M ZnI₂, respectively.

The transference number of Zn²⁺ ($t_{Zn^{2+}}$) was calculated based on the CA at polarization voltage of 100 mV and corresponding EIS spectra before and after the polarization in the Zn/Zn cells.^{2,3} The formula is as follows:

$$t_{Zn^{2+}} = \frac{I^s R_b^s (\Delta V - I^0 R_i^0)}{I^0 R_b^0 (\Delta V - I^s R_i^s)}$$

in which ΔV and I^0, I^s represent to polarization voltage (V) and currents (A) in initial, steady during the CA. The R_b^0, R_b^s and R_i^0, R_i^s correspond to bulk and interfacial resistances (Ω) between electrolyte and electrode in initial and steady state, respectively, which were fitted by EIS spectra.

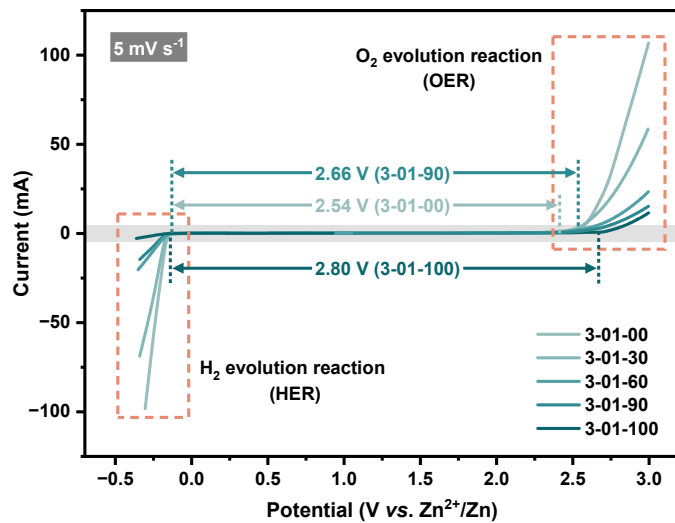


Figure S6. LSV curves at 5 mV s^{-1} in Zn/SS cells used electrolytes with gradient EG/H₂O solvent containing 3 M $\text{Zn}(\text{CF}_3\text{SO}_3)_2$ and 0.1 M ZnI_2 , respectively.

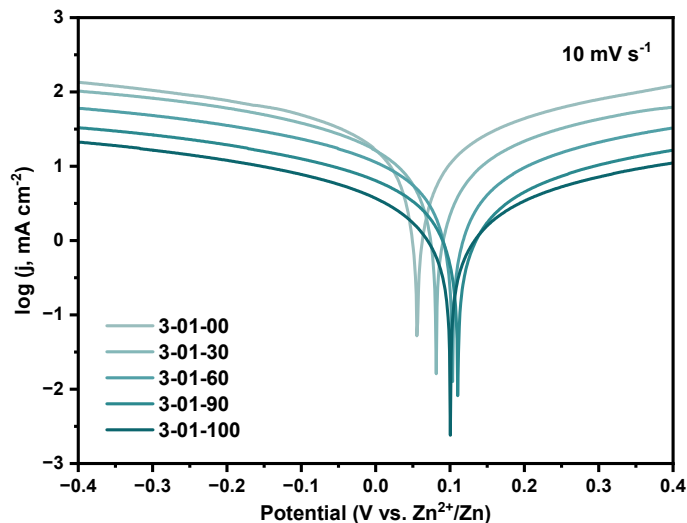


Figure S7. Tafel curves at 10 mV s^{-1} of solutions with gradient EG/H₂O solvents, respectively.

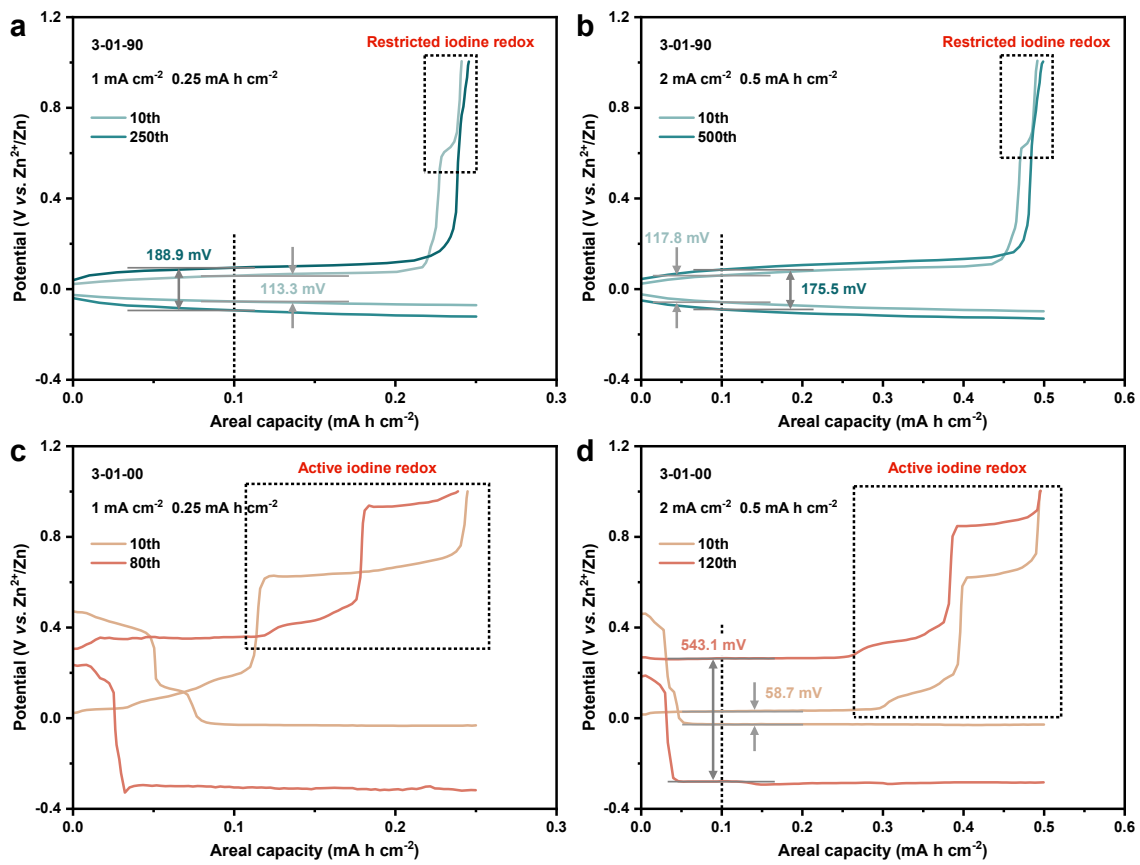


Figure S8. Galvanostatic voltage curves at $1, 2 \text{ mA cm}^{-2}$ of Zn/Cu cells with (a, b) 3-01-90 and (c, d) 3-01-00, respectively.

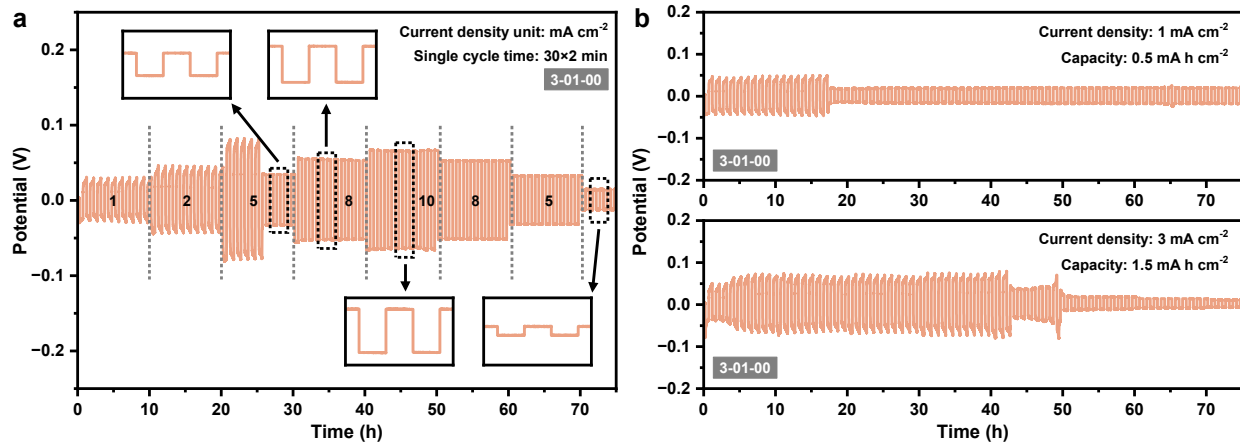


Figure S9. Galvanostatic (a) rate capability between 1 to 10 mA cm^{-2} and (b) cycling performances at $0.5, 1.5 \text{ mA cm}^{-2}$ of Zn/Zn cells with 3-01-00, respectively.

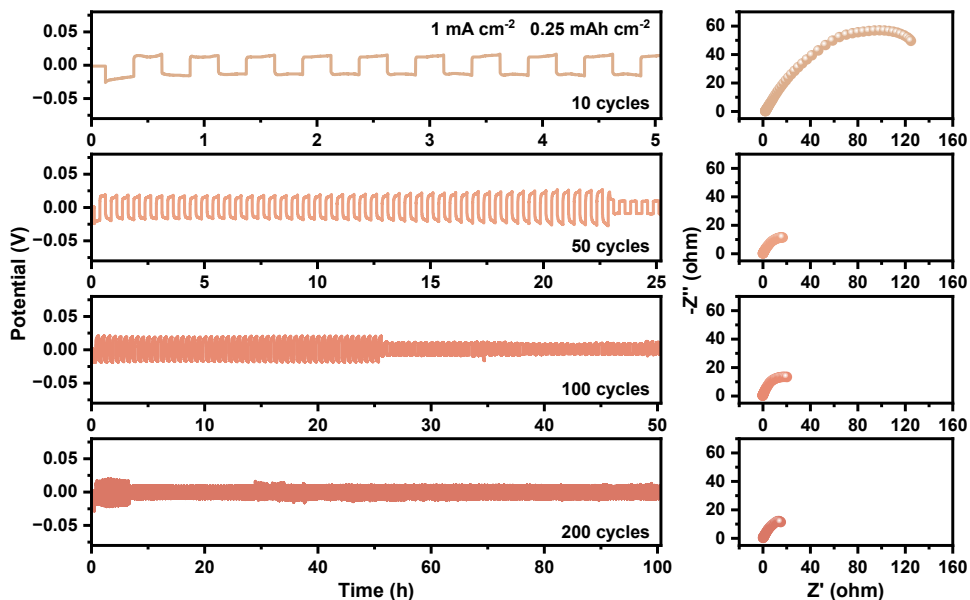


Figure S10. Galvanostatic cycling performances at 1 mA cm^{-2} to $0.25 \text{ mA h cm}^{-2}$ and corresponding EIS spectra in the different cycles of Zn/Zn cells with 3-01-00, respectively.

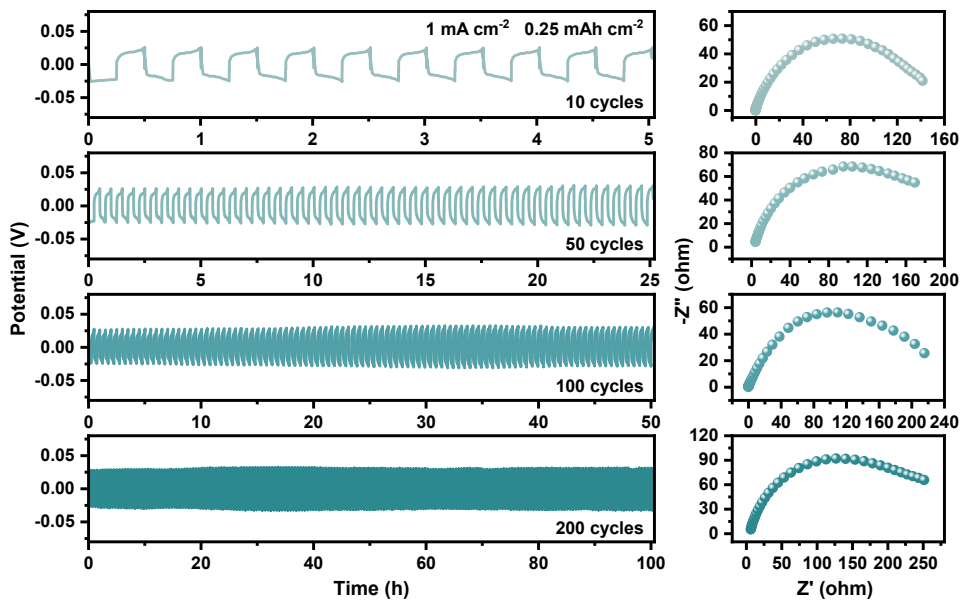


Figure S11. Galvanostatic cycling performances at 1 mA cm^{-2} to $0.25 \text{ mA h cm}^{-2}$ and corresponding EIS spectra in the different cycles of Zn/Zn cells with 3–01–90, respectively.

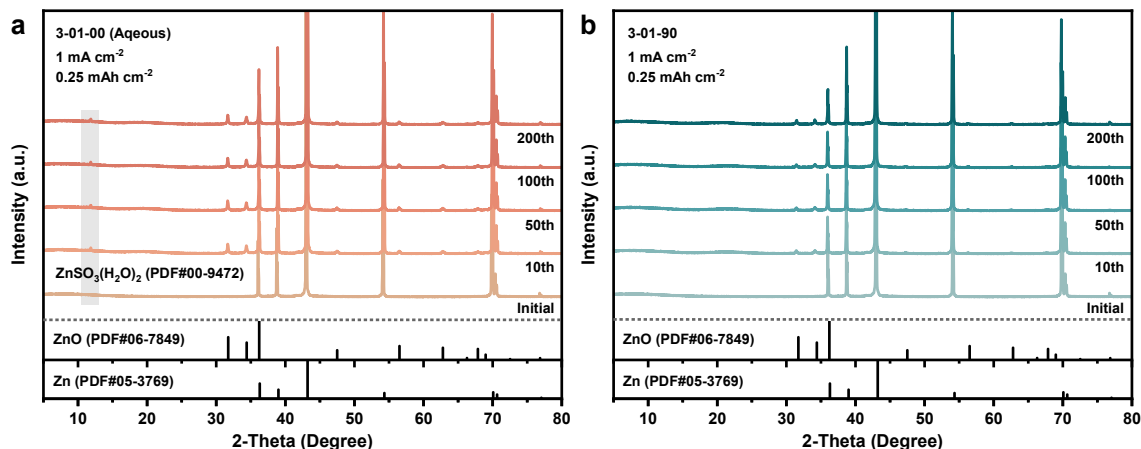


Figure S12. XRD patterns in the different cycles at 1 mA cm^{-2} to $0.25 \text{ mA h cm}^{-2}$ of Zn/Zn cells with (a) 3–01–00 and (b) 3–01–90, respectively.

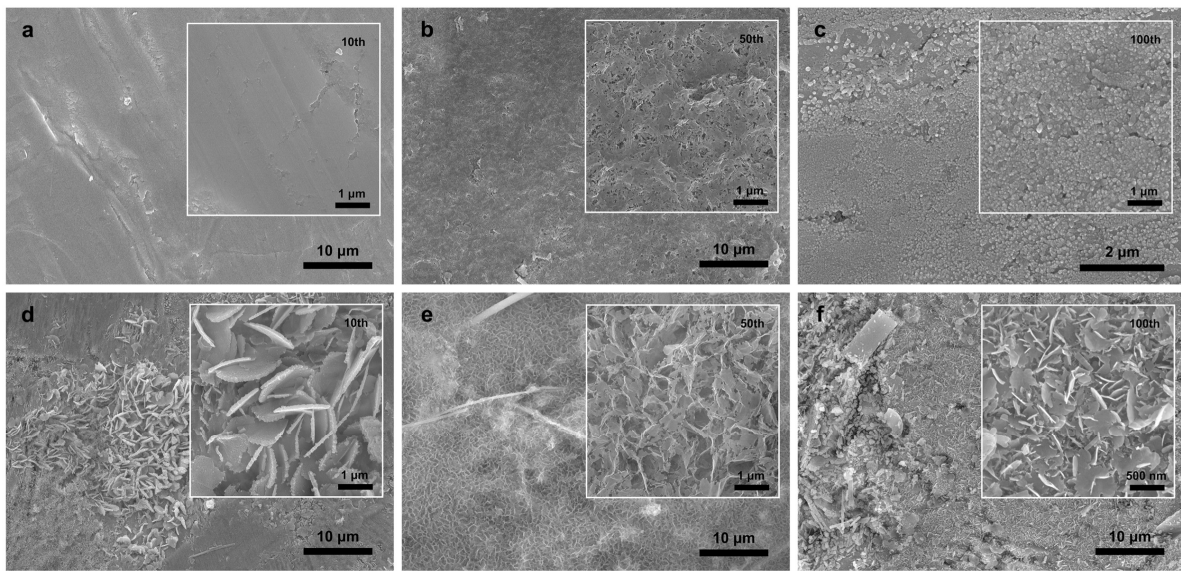


Figure S13. SEM images in the different cycles at 1 mA cm^{-2} to $0.25 \text{ mA h cm}^{-2}$ of Zn/Zn cells with (a–c) 3–01–90 and (d–f) 3–01–00, respectively.

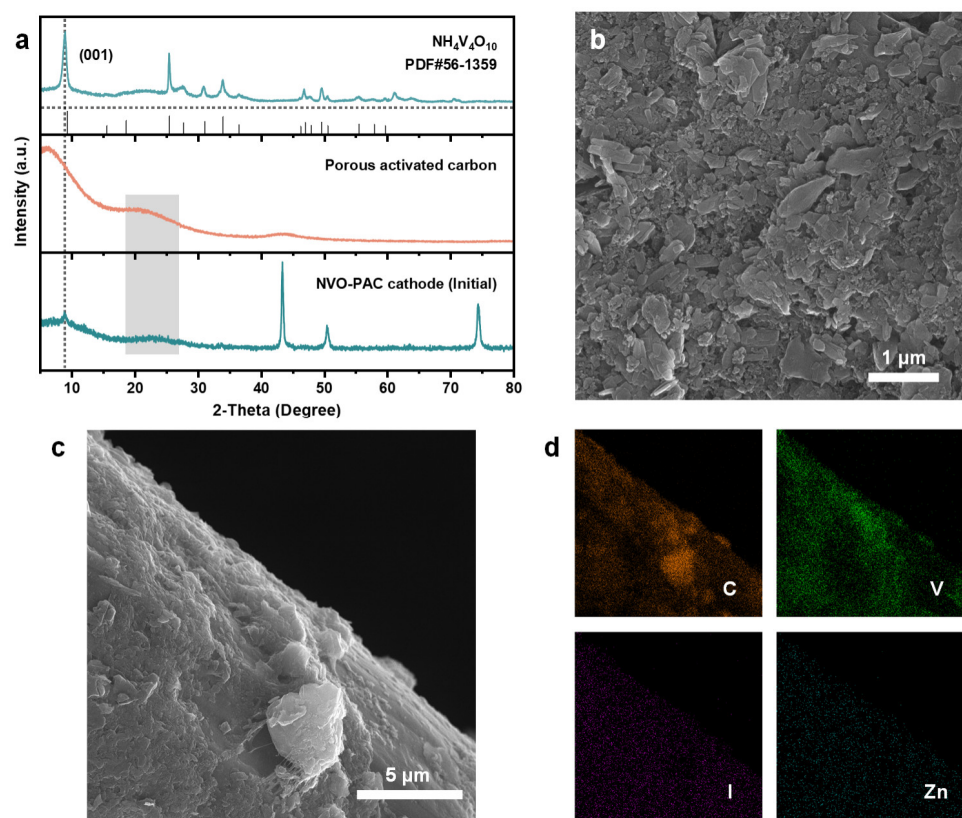


Figure S14. (a) XRD patterns of NVO, PAC powders and NVO–PAC electrode, respectively. (b–d) SEM images and corresponding EDS elemental mappings of NVO–PAC electrode.

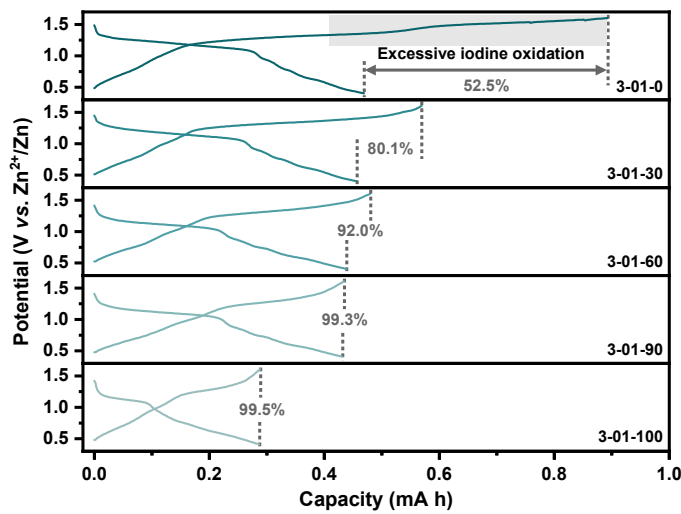


Figure S15. GCD curves at 1 A g^{-1} of Zn/NVO-PAC cells used electrolytes with gradient EG/ H_2O solvent containing 3 M $\text{Zn}(\text{CF}_3\text{SO}_3)_2$ and 0.1 M ZnI_2 , respectively.

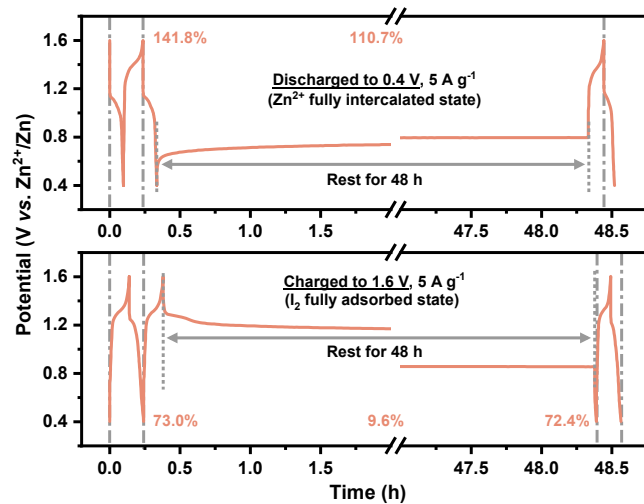


Figure S16. Rest tests for 48 h from the fully discharged and charged states of Zn/NVO-PAC cell with 3-01-00, respectively.

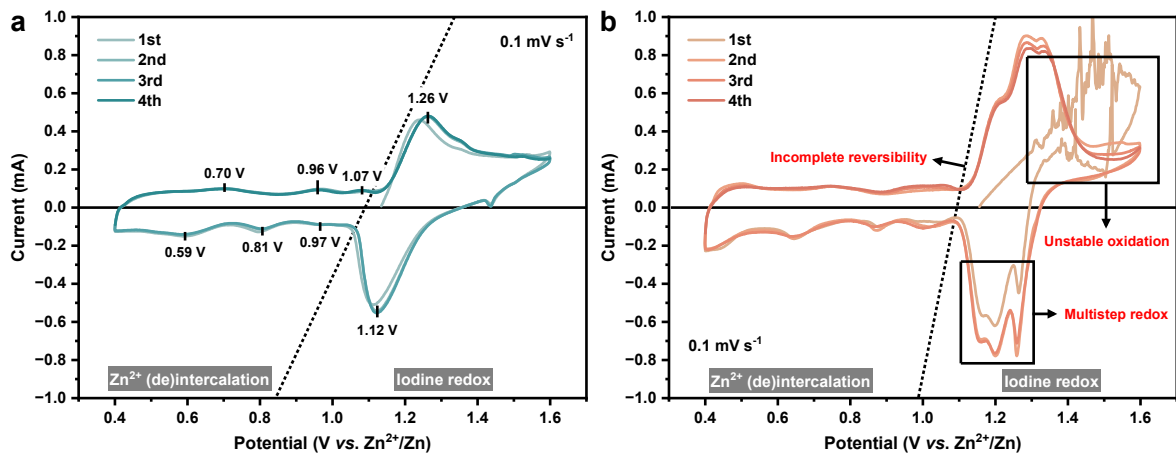


Figure S17. CV curves at 0.1 mV s^{-1} of Zn/NVO-PAC cells with (a) 3-01-90 and (b) 3-01-00, respectively.

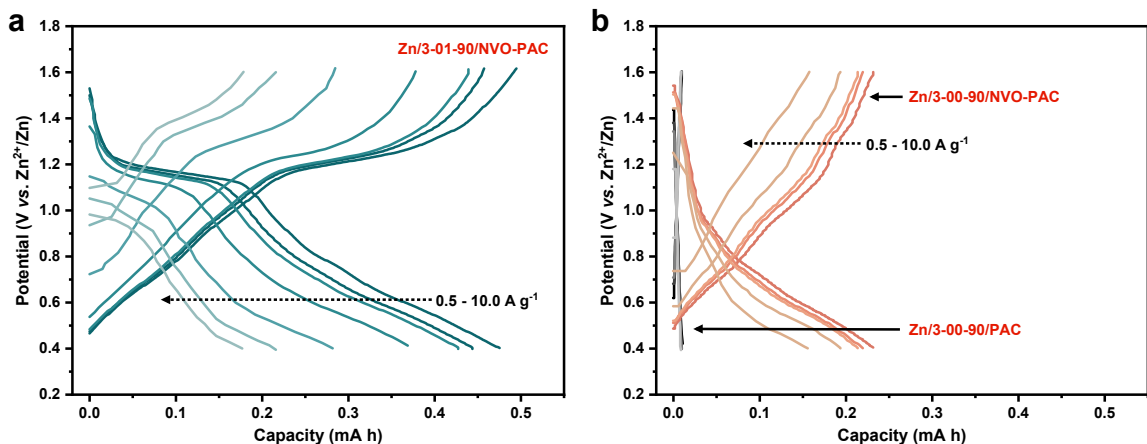


Figure S18. GCD curves at 0.5 to 10.0 A g^{-1} of (a) Zn/3-01-90/NVO-PAC cell, (b) Zn/3-00-90/NVO-PAC and Zn/3-00-90/PAC cells, respectively.

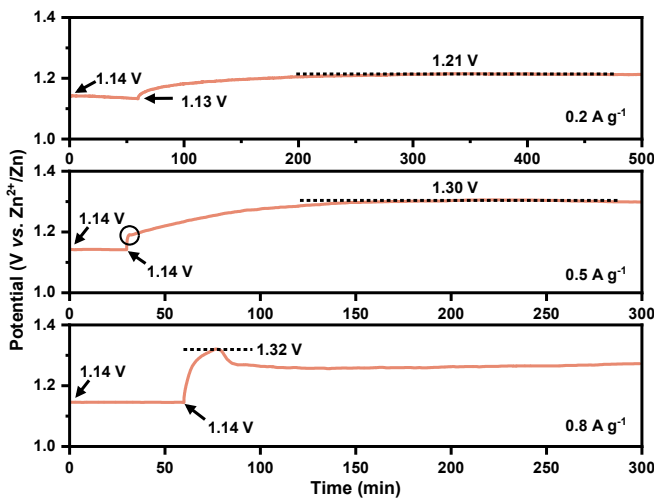


Figure S19. GCD curves at $0.2, 0.5, 0.8 \text{ A g}^{-1}$ of Zn/NVO-PAC cells with 3–01–00, respectively.

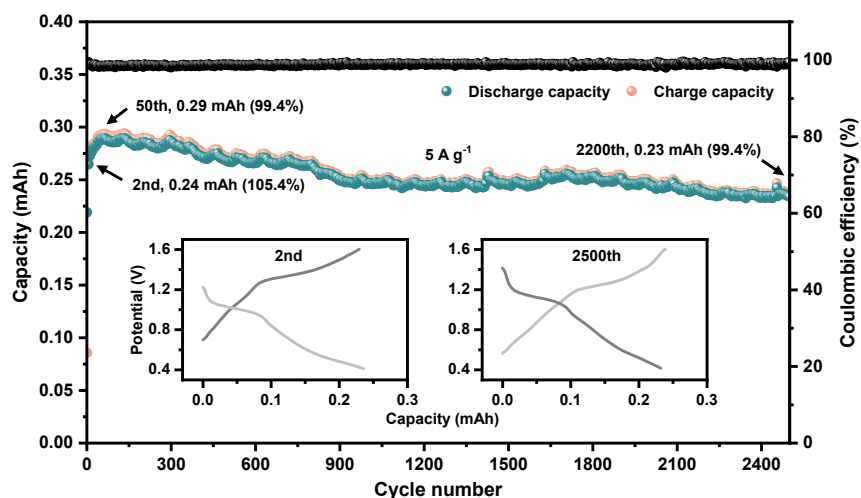


Figure S20. Long-term cycling performance at 2 A g^{-1} of Zn/NVO-PAC cell with 3–01–90.

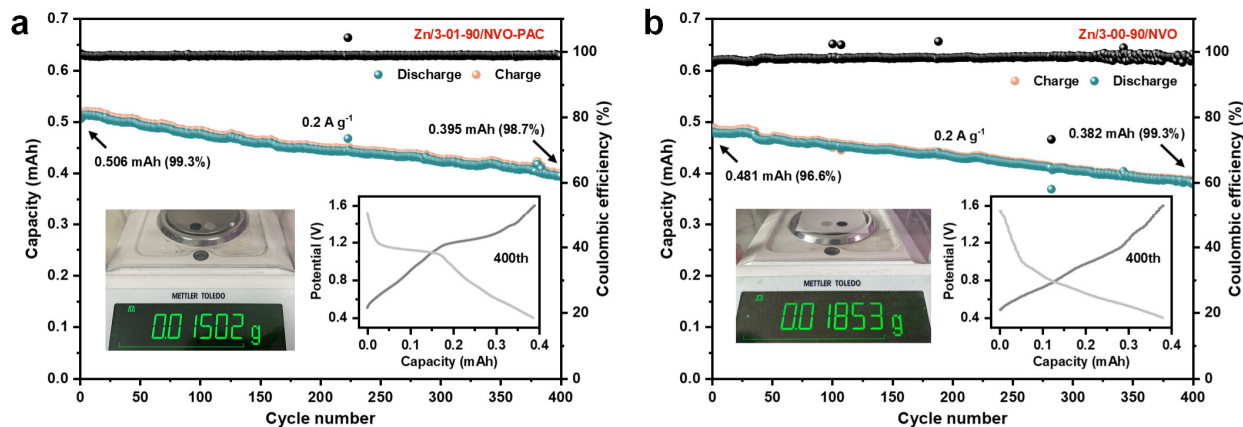


Figure S21. Cycling performance at 0.2 A g^{-1} of lightweight (a) Zn/NVO-PAC cell with 3-01-90 and (b) Zn/NVO cell with 3-00-90 (the zinc foil and graphite paper in thicknesses of 10 and 25 μm , respectively).

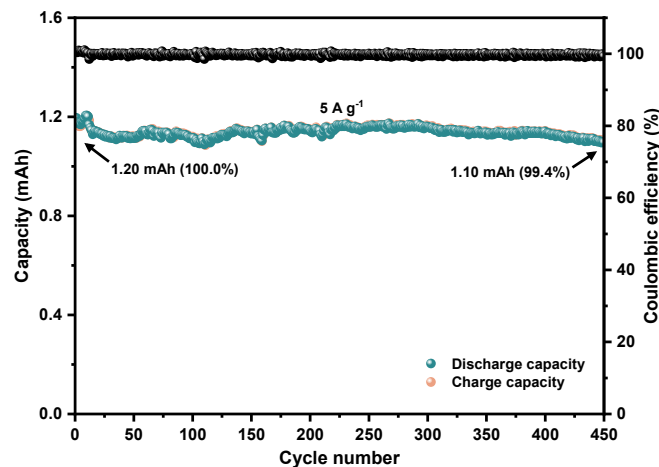


Figure S22. Cycling performance at 5 A g^{-1} of Zn/NVO-PAC pouch cell with 3-01-90 (the cathodic area is $3 \times 3 \text{ cm}^2$).

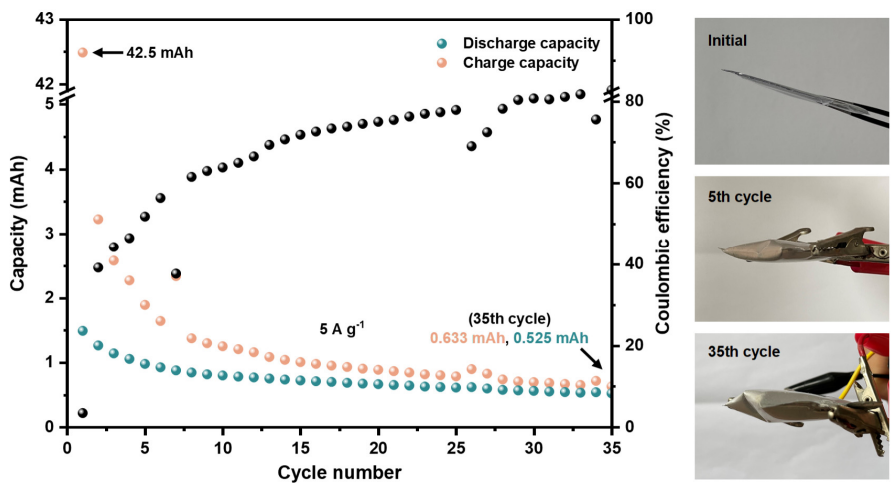


Figure S23. Cycling performance and optical images in the different cycles at 5 A g^{-1} of Zn/NVO–PAC pouch cell with 3–01–00.

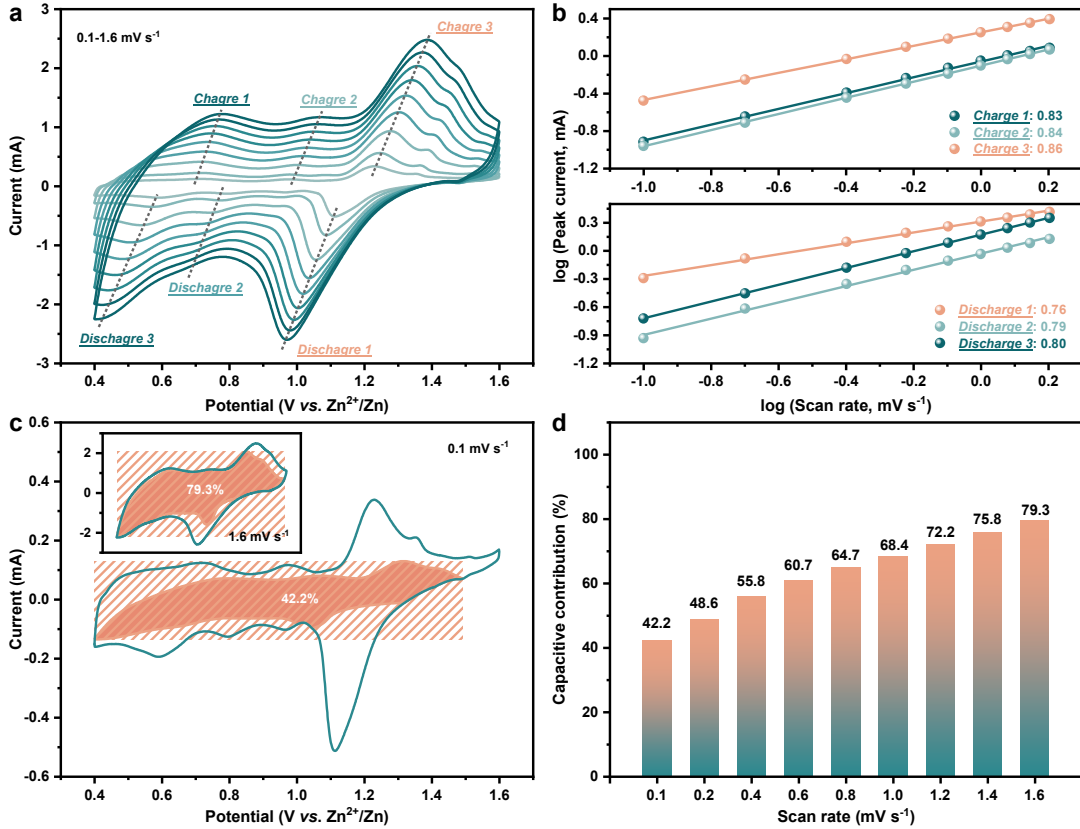


Figure S24. (a) CV curves at the scan rates from 0.1 to 1.0 mV s^{-1} , (b) the corresponding $\log(\text{current})$ vs. $\log(\text{scan rate})$ plots of redox peaks. (c) marked region of capacitive–controlled contribution at 0.1 and 1.6 mV s^{-1} and (d) calculated capacitive–controlled contribution of Zn/NVO–PAC cell with 3–01–90.

According to the researches of Dunn⁴, the current and scan rate in CV curves have relationship with equations: $i = av^b$; $\log(i) = b \times \log(v) + \log(a)$. Where a , b are adjustable parameters and the b value is between 0.5 and 1 , in which the b value of 0.5 indicates a full diffusion–controlled process and b value of 1 corresponds to the full capacitive contribution. Also, the values of b can be obtained by calculating the slope of the $\log(i)$ vs. $\log(v)$ plots.

Meanwhile, the contribution of pseudocapacitive can be quantified by the equations: $i = k_1v + k_2v^{1/2}$; $i/v^{1/2} = k_1v^{1/2} + k_2$.⁴⁻⁶ Where the capacity contribution can be divided into capacitive (measured with k_1) and diffusion–controlled (measured with k_2). By determining values of both k_1 and k_2 , we can distinguish the fraction of the current from surface capacitance and diffusion limited.⁷

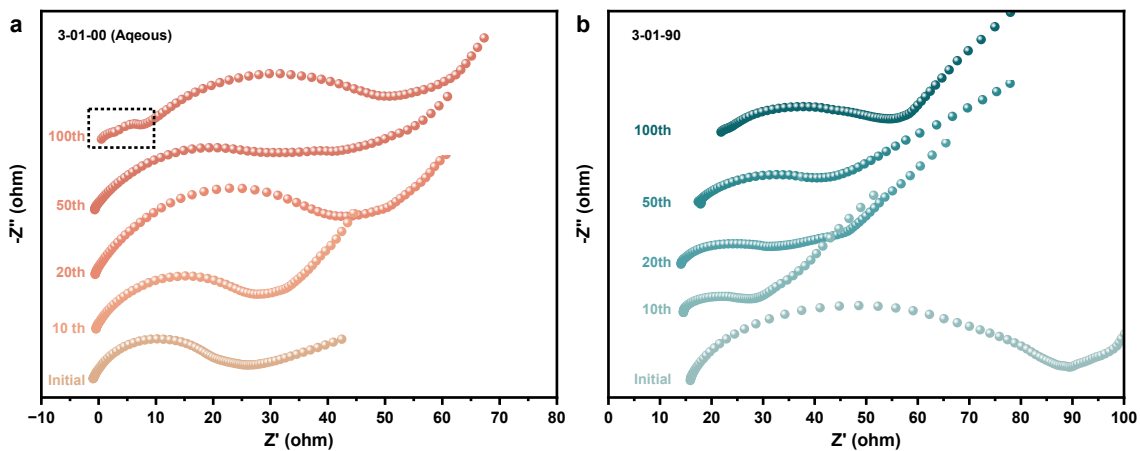


Figure S25. *Ex-situ* EIS spectra of Zn/NVO–PAC cells with 3–01–00 and 3–01–90, respectively.

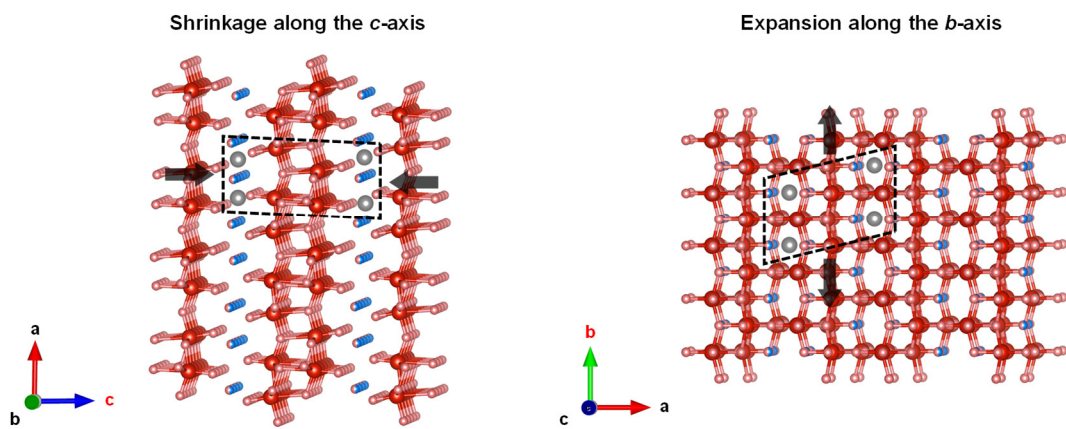


Figure S26. Schematic diagrams of Zn^{2+} intercalation in the NVO projected along the b - and c -axes, respectively.

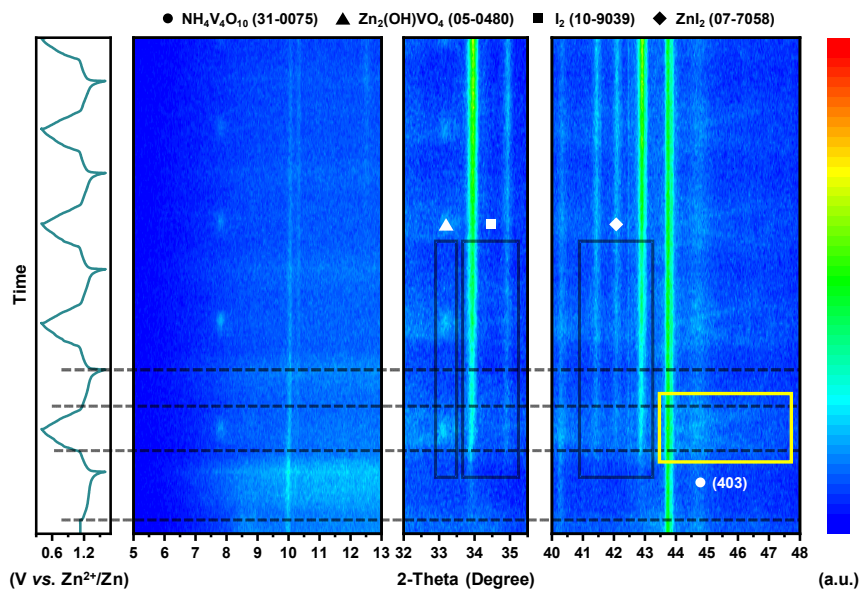


Figure S27. *In-situ* XRD pattern of cathode in Zn/NVO–PAC cell with 3–01–00.

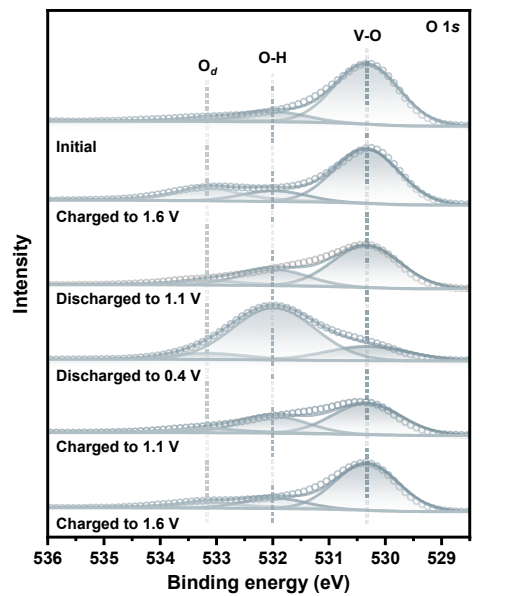


Figure S28. *Ex-situ* XPS O 1s spectra of cathode in Zn/NVO–PAC cell with 3–01–90.

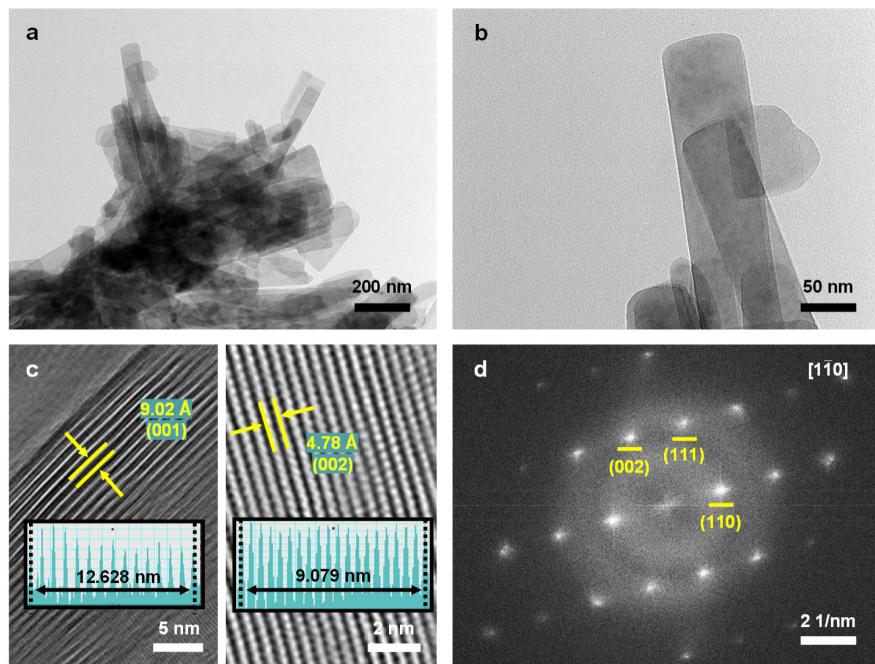


Figure S29. (a, b) TEM, (c) HRTEM images and (d) corresponding SAED patterns of NVO powder.



Figure S30. Optical images in the different states of Zn/NVO-PAC cuvette cells with (a) 3-01-90 and (b) 3-01-00, respectively.

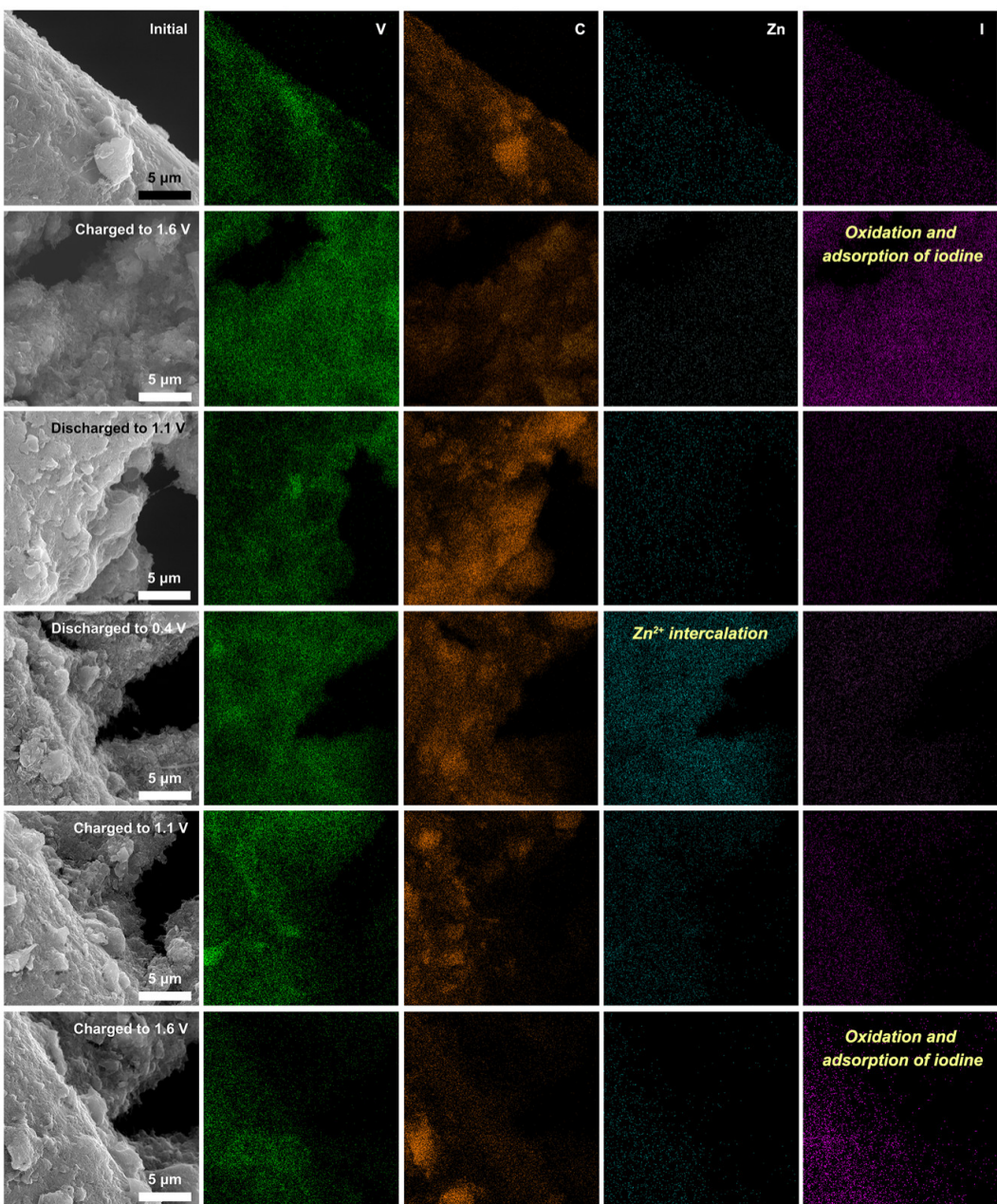


Figure S31. SEM images and corresponding elemental mappings in the different states of cathode in Zn/NVO–PAC cells with 3–01–90.

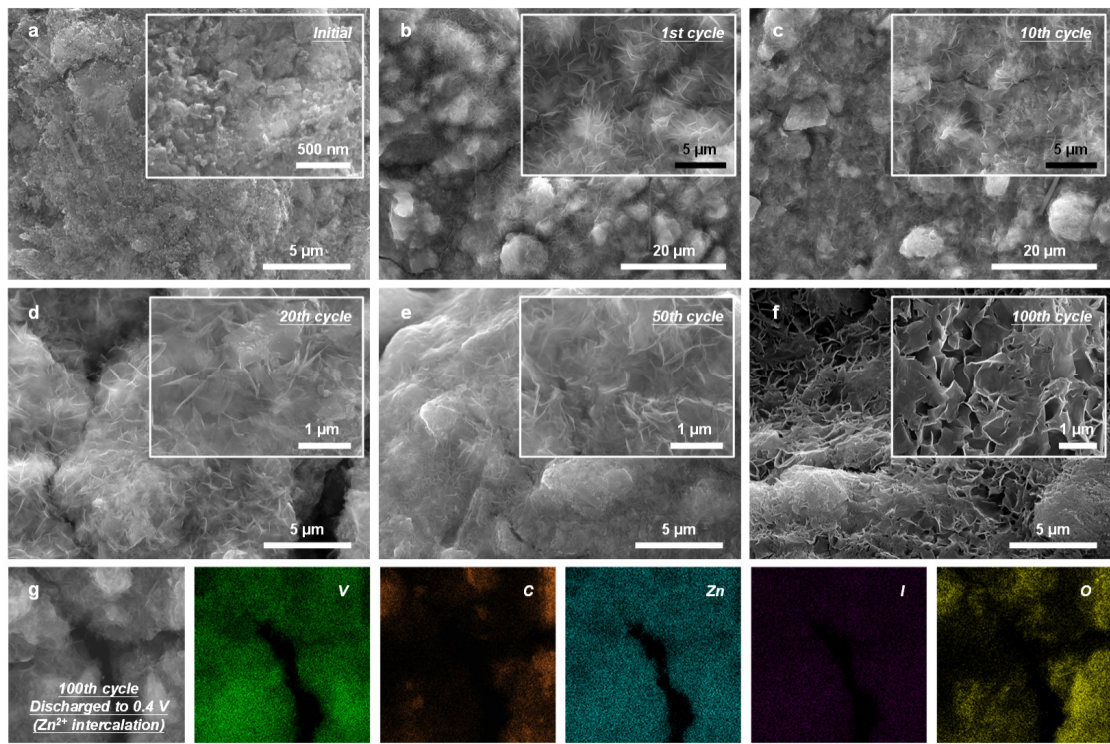


Figure S32. (a–f) SEM images in the different cycles and (g) additional EDS elemental mappings at the fully discharged to 0.4 V in the 100th cycle of cathode in Zn/NVO–PAC cells with 3–01–90.

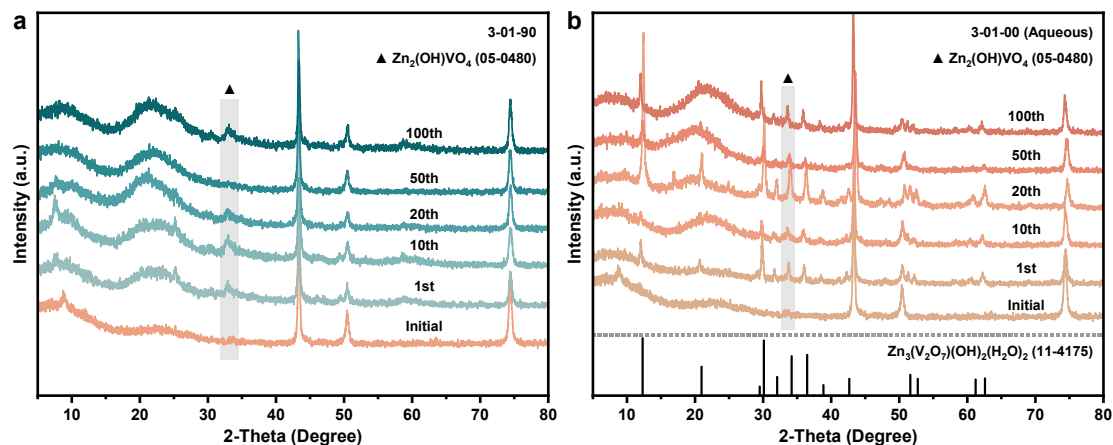


Figure S33. XRD patterns in the different cycles of cathode in Zn/NVO–PAC cells with (a) 3–01–90 and (b) 3–01–00, respectively.

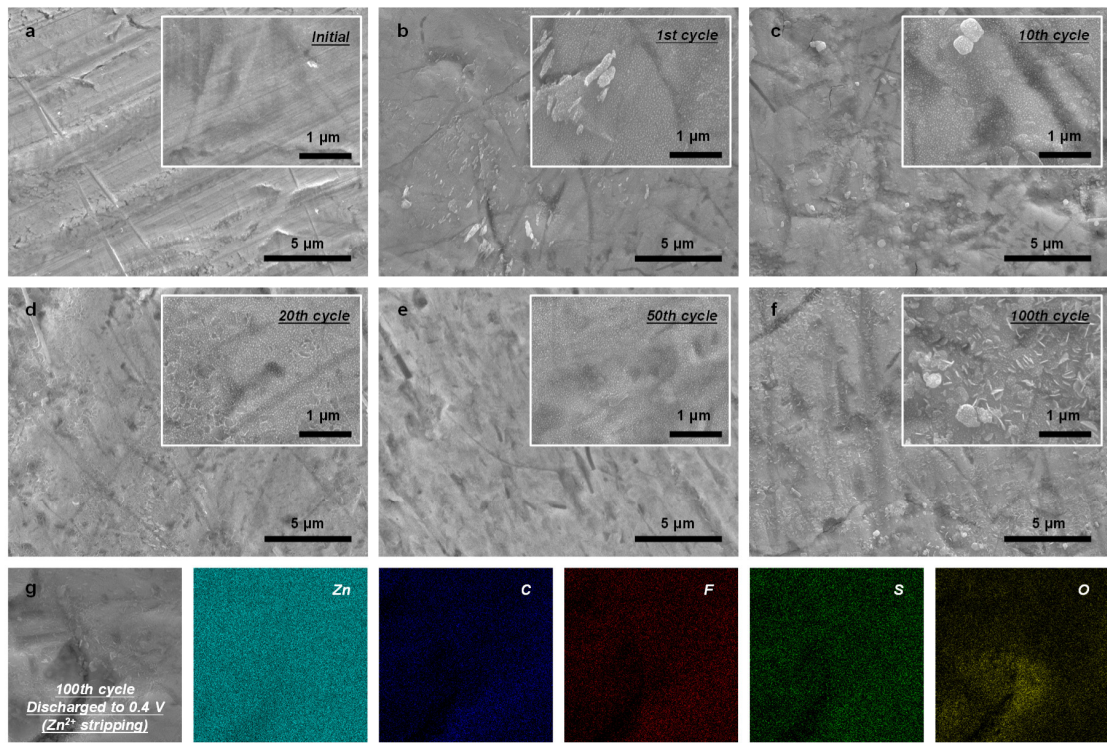


Figure S34. (a–f) SEM images in the different cycles and (g) additional EDS elemental mappings at fully discharged to 0.4 V in the 100th cycle of anode in Zn/NVO–PAC cells with 3–01–90.

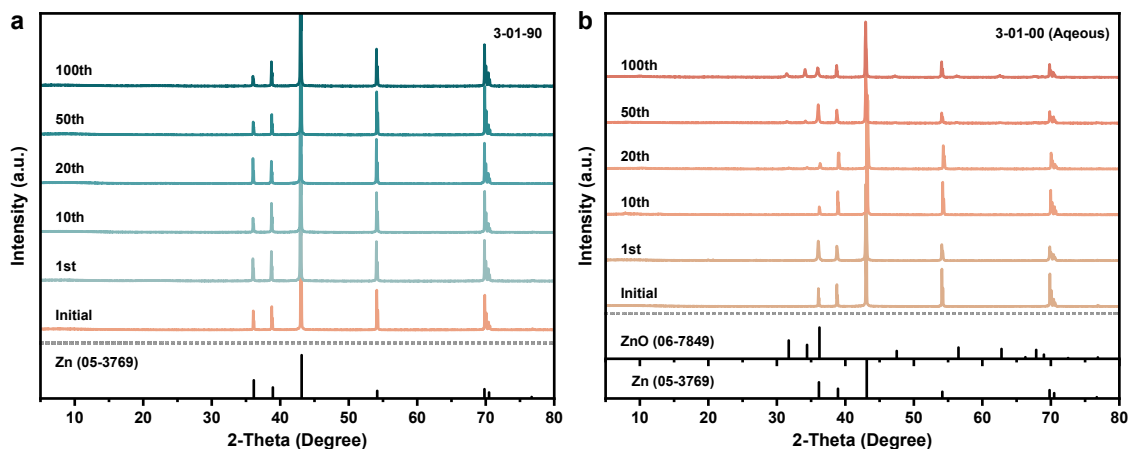


Figure S35. XRD patterns in the different cycles of anode in Zn/NVO–PAC cells with (a) 3–01–90 and (b) 3–01–00, respectively.

Table S1. Equilibrium potential and corrosion current calculated based on Tafel curves at 10 mV s^{-1} (**Fig. S7**) of solutions with gradient EG/H₂O solvents, respectively.

Electrolyte	Equilibrium potential (mV)	Corrosion current (mA)
3-01-00	56	12.01
3-01-30	82	8.31
3-01-60	104	4.9
3-01-90	111	2.85
3-01-100	101	2.11

Table S2. Electrochemical performances of cathodes with ion(s)–(de)intercalation (vanadium–based, manganese–based, molybdenum–based and Prussian–blue analogous) and *in*–*situ* iodine redox in zinc–based batteries.

Material	Electrolyte	Discharge medium voltage (V vs. Zn ²⁺ /Zn)	Specific capacity (mA h g ⁻¹)	Ref.
δ –V ₂ O ₅	3 M Zn(CF ₃ SO ₃) ₂	0.61 (0.2–1.6)	215.6 (1 A g ⁻¹)	8
a –V ₂ O ₅ @C	3 M Zn(CF ₃ SO ₃) ₂	0.70 (0.3–1.9)	565.7 (1 A g ⁻¹)	9
V ₂ O ₅ @PEDOT/CC	2.5 M Zn(CF ₃ SO ₃) ₂	0.59 (0.2–1.6)	273.9 (1 A g ⁻¹)	10
O _d –V ₆ O ₁₃	3M Zn(CH ₃ F ₃ SO ₃) ₂	0.61 (0.2–1.5)	319.1 (1 A g ⁻¹)	11
Ca _{0.25} V ₂ O ₅ · <i>n</i> H ₂ O	1 M ZnSO ₄	0.78 (0.6–1.6)	267.2 (1.6 A g ⁻¹)	12
Zn _{0.25} V ₂ O ₅ · <i>n</i> H ₂ O	1 M ZnSO ₄	0.61 (0.5–1.4)	266.7 (1.2 A g ⁻¹)	13
Li _x V ₂ O ₅ · <i>n</i> H ₂ O	2 M ZnSO ₄	0.57 (0.4–1.4)	386.8 (1 A g ⁻¹)	14
Mn _x V ₂ O ₅ · <i>n</i> H ₂ O	3 M Zn(CF ₃ SO ₃) ₂	0.70 (0.2–1.6)	345.9 (1 A g ⁻¹)	15
MnV ₂ O ₄	3 M Zn(CF ₃ SO ₃) ₂	0.72 (0.2–1.8)	418.7 (1 A g ⁻¹)	16
δ –Ni _{0.25} V ₂ O ₅ · <i>n</i> H ₂ O	3 M ZnSO ₄	0.68 (0.3–1.7)	287.9 (1 A g ⁻¹)	17
(Na,Mn)V ₈ O ₂₀ · <i>n</i> H ₂ O	3 M Zn(CF ₃ SO ₃) ₂	0.61 (0.3–1.25)	249.6 (1 A g ⁻¹)	18
([N(CH ₃) ₄] _{0.77} ,Zn _{0.23})V ₈ O ₂₀ ·3.8H ₂ O	3 M Zn(CF ₃ SO ₃) ₂	0.66 (0.3–1.5)	275.2 (1 A g ⁻¹)	19
VOPO ₄ ·2H ₂ O	2 M Zn(CF ₃ SO ₃) ₂	1.02 (0.2–1.9)	235.0 (1 A g ⁻¹)	20
VS ₂	1 M ZnSO ₄	0.58 (0.4–1.0)	114.8 (1 A g ⁻¹)	7
VSe ₂	2 M ZnSO ₄	0.66 (0.2–1.6)	93.3 (1 A g ⁻¹)	21
MnO ₂ · <i>n</i> H ₂ O	1 M ZnSO ₄	1.32 (1.0–1.9)	228.9 (1 A g ⁻¹)	22
δ –MnO ₂	1 M Zn(TFSI) ₂ + 0.1 M Mn(TFSI) ₂	1.32 (1.0–1.8)	171.2 (1.5 A g ⁻¹)	23
α –MnO ₂	2 M ZnSO ₄ + 0.1 M MnSO ₄	1.32 (1.0–1.85)	205.4 (1.5 A g ⁻¹)	24
β –MnO ₂	3 M Zn(CF ₃ SO ₃) ₂ + 0.1 M Mn(CF ₃ SO ₃) ₂	1.30 (0.8–1.9)	188.0 (1 A g ⁻¹)	25
O _d –MnO ₂	1 M ZnSO ₄ + 0.2 M MnSO ₄	1.36 (1.0–1.8)	234.0 (1 A g ⁻¹)	26
a –K _x MnO ₂	2 M ZnSO ₄ + 0.1 M MnSO ₄	1.36 (0.9–1.8)	272.7 (1 A g ⁻¹)	27
Cu–MnO ₂ · <i>n</i> H ₂ O	2 M ZnSO ₄ + 0.1 M MnSO ₄	1.36 (1.0–1.8)	195.8 (1 A g ⁻¹)	28
Ca _{0.28} MnO ₂ ·0.5H ₂ O	1 M ZnSO ₄ + 0.1 M MnSO ₄	1.32 (0.4–1.9)	180.6 (1 A g ⁻¹)	29

O _d ⁻ K _{0.8} Mn ₈ O ₁₆	2 M ZnSO ₄ + 0.1 M MnSO ₄	1.31 (0.8–1.8)	132.1 (1 A g ⁻¹)	³⁰
PANI–MnO ₂	2 M ZnSO ₄ + 0.1 M MnSO ₄	1.34 (1.0–1.8)	187.6 (1 A g ⁻¹)	³¹
MnO ₂ /MnZn–BTC	3 M ZnSO ₄	1.26 (0.6–1.9)	112.8 (1 A g ⁻¹)	³²
Ni _x Mn ₂ O ₃	2 M ZnSO ₄	1.30 (0.8–1.8)	122.8 (1 A g ⁻¹)	³³
Co[Co _{1/4} Fe _{3/4} (CN) ₆]–I ₂	2 M ZnSO ₄	1.24 (0.5–1.6)	185.9 (1 A g ⁻¹)	³⁴
Nb ₂ CT _x –I ₂	1 M ZnSO ₄	1.26 (0.4–1.6)	208.3 (1 A g ⁻¹)	³⁵
Ti ₃ C ₂ I ₂	2 M ZnCl ₂ + 1 M KCl	1.27 (0.8–1.8)	188.3 (1 A g ⁻¹)	³⁶
PAC–I ₂	19 M ZnCl ₂ + 19 M LiCl + 8 M Acetonitrile	1.20 (0.6–1.8)	491.7 (1 A g ⁻¹)	³⁷
MoS ₂ /Graphene (G)	2 M Zn(CF ₃ SO ₃) ₂	0.51 (0.2–1.5)	228.2 (1 A g ⁻¹)	³⁸
E–MoS ₂	2 M ZnSO ₄	0.51 (0.3–1.5)	167.4 (1 A g ⁻¹)	³⁹
MoS ₂	3 M Zn(CF ₃ SO ₃) ₂	0.58 (0.2–1.3)	205.5 (1 A g ⁻¹)	⁴⁰
K _{1.34} Co _{0.23} Mn _{0.88} [Fe–(CN) ₆]	2 M Zn(CF ₃ SO ₃) ₂	1.27 (0.5–1.8)	55.5 (1 A g ⁻¹)	⁴¹
CoFe(CN) ₆	4 M Zn(CF ₃ SO ₃) ₂	1.69 (0.8–1.9)	154.1 (1 A g ⁻¹)	⁴²

Table S3. The fitting ohmic resistances (R_s) and charge transfer resistances (R_{ct}) from the EIS spectra (Fig. S25) of Zn/NVO–PAC cells with 3–01–00 and 3–01–90, respectively.

Electrolyte	Cycle	R_s (Ω)	R_{ct} (Ω)
3–01–00	Initial	0.9	26.6
	10th	1.1	48.4
	20th	1.3	60.2
	50th	1.5	39.2
	100th	1.7	70.7
3–01–90	Initial	15.6	67.3
	10th	14.4	14.9
	20th	14.0	20.4
	50th	17.1	32.1
	100th	22.2	31.7

References

1. B. Y. Tang, J. Zhou, G. Z. Fang, F. Liu, C. Y. Zhu, C. Wang, A. Q. Pan and S. Q. Liang, *J. Mater. Chem. A*, 2019, **7**, 940-945.
2. J. Evans, C. A. Vincent and P. G. Bruce, *Polymer*, 1987, **28**, 2324-2328.
3. K. M. Abraham, Z. Jiang and B. Carroll, *Chem. Mater.*, 1997, **9**, 1978-1988.
4. J. Wang, J. Polleux, J. Lim and B. Dunn, *J. Phys. Chem. C*, 2007, **111**, 14925-14931.
5. T. Brezesinski, J. Wang, S. H. Tolbert and B. Dunn, *Nat. Mater.*, 2010, **9**, 146-151.
6. D. Chao, C. Zhu, P. Yang, X. Xia, J. Liu, J. Wang, X. Fan, S. V. Savilov, J. Lin, H. J. Fan and Z. X. Shen, *Nat. Commun.*, 2016, **7**, 12122.
7. P. He, M. Y. Yan, G. B. Zhang, R. M. Sun, L. N. Chen, Q. Y. An and L. Q. Mai, *Adv. Energy Mater.*, 2017, **7**, 1601920.
8. X. Liu, H. Euchner, M. Zarzabeitia, X. Gao, G. A. Elia, A. Gross and S. Passerini, *ACS Energy Lett.*, 2020, **5**, 2979-2986.
9. S. Deng, Z. Yuan, Z. Tie, C. Wang, L. Song and Z. Niu, *Angew. Chem. Int. Ed.*, 2020, **59**, 22002-22006.
10. D. Xu, H. Wang, F. Li, Z. Guan, R. Wang, B. He, Y. Gong and X. Hu, *Adv. Mater. Interfaces*, 2018, **6**, 1801506.
11. M. Liao, J. Wang, L. Ye, H. Sun, Y. Wen, C. Wang, X. Sun, B. Wang and H. Peng, *Angew. Chem. Int. Ed.*, 2020, **59**, 2273-2278.
12. C. Xia, J. Guo, P. Li, X. Zhang and H. N. Alshareef, *Angew. Chem. Int. Ed.*, 2018, **57**, 3943-3948.
13. D. Kundu, B. D. Adams, V. Duffort, S. H. Vajargah and L. F. Nazar, *Nat. Energy*, 2016, **1**, 16119.
14. Y. Yang, Y. Tang, G. Fang, L. Shan, J. Guo, W. Zhang, C. Wang, L. Wang, J. Zhou and S. Liang, *Energy Environ. Sci.*, 2018, **11**, 3157-3162.
15. C. F. Liu, Z. Neale, J. Q. Zheng, X. X. Jia, J. J. Huang, M. Y. Yan, M. Tian, M. S. Wang, J. H. Yang and G. Z. Cao, *Energy Environ. Sci.*, 2019, **12**, 2273-2285.
16. S. Q. Wei, S. M. Chen, X. Z. Su, Z. H. Qi, C. D. Wang, B. B. Ganguli, P. J. Zhang, K. F. Zhu, Y. Y. Cao, Q. He, D. F. Cao, X. Guo, W. Wen, X. J. Wu, P. M. Ajayan and L. Song, *Energy Environ. Sci.*, 2021, **14**, 3954-3964.
17. J. Li, K. McColl, X. Lu, S. Sathasivam, H. Dong, L. Kang, Z. Li, S. Zhao, A. G. Kafizas, R. Wang, D. J. L. Brett, P. R. Shearing, F. Corà, G. He, C. J. Carmalt and I. P. Parkin, *Adv. Energy Mater.*, 2020, **10**, 2000058..
18. M. Du, C. Liu, F. Zhang, W. Dong, X. Zhang, Y. Sang, J. J. Wang, Y. G. Guo, H. Liu and S. Wang, *Adv. Sci.*, 2020, **7**, 2000083.
19. F. Zhang, X. Sun, M. Du, X. Zhang, W. Dong, Y. Sang, J. Wang, Y. Li, H. Liu and S. Wang, *Energy Environ. Mater.*, 2021, **4**, 620-630.
20. L. F. Hu, Z. Y. Wu, C. J. Lu, F. Ye, Q. Liu and Z. M. Sun, *Energy Environ. Sci.*, 2021, **14**, 4095-4106.
21. Z. Wu, C. Lu, Y. Wang, L. Zhang, L. Jiang, W. Tian, C. Cai, Q. Gu, Z. Sun and L. Hu, *Small*, 2020, **16**, e2000698.
22. K. W. Nam, H. Kim, J. H. Choi and J. W. Choi, *Energy Environ. Sci.*, 2019, **12**, 1999-2009.

23. Y. Jin, L. Zou, L. Liu, M. H. Engelhard, R. L. Patel, Z. Nie, K. S. Han, Y. Shao, C. Wang, J. Zhu, H. Pan and J. Liu, *Adv. Mater.*, 2019, **31**, e1900567.
24. H. L. Pan, Y. Y. Shao, P. F. Yan, Y. W. Cheng, K. S. Han, Z. M. Nie, C. M. Wang, J. H. Yang, X. L. Li, P. Bhattacharya, K. T. Mueller and J. Liu, *Nat. Energy*, 2016, **1**, 16039.
25. N. Zhang, F. Cheng, J. Liu, L. Wang, X. Long, X. Liu, F. Li and J. Chen, *Nat. Commun.*, 2017, **8**, 405.
26. T. Xiong, Z. G. Yu, H. J. Wu, Y. H. Du, Q. D. Xie, J. S. Chen, Y. W. Zhang, S. J. Pennycook, W. S. V. Lee and J. M. Xue, *Adv. Energy Mater.*, 2019, **9**, 1803815.
27. K. Han, F. Q. An, F. S. Yan, H. L. Chen, Q. Wan, Y. C. Liu, P. Li and X. H. Qu, *J. Mater. Chem. A*, 2021, **9**, 15637-15647.
28. F. W. Fenta, B. W. Olbasa, M. C. Tsai, M. A. Weret, T. A. Zegeye, C. J. Huang, W. H. Huang, T. S. Zeleke, N. A. Sahalie, C. W. Pao, S. H. Wu, W. N. Su, H. J. Dai and B. J. Hwang, *J. Mater. Chem. A*, 2020, **8**, 17595-17607.
29. T. Sun, Q. Nian, S. Zheng, J. Shi and Z. Tao, *Small*, 2020, **16**, e2000597.
30. G. Z. Fang, J. Zhou, A. Q. Pan and S. Q. Liang, *ACS Energy Lett.*, 2018, **3**, 2480-2501.
31. J. Huang, Z. Wang, M. Hou, X. Dong, Y. Liu, Y. Wang and Y. Xia, *Nat. Commun.*, 2018, **9**, 2906.
32. Y. Liu, Z. Qin, X. Yang and X. Sun, *Adv. Funct. Mater.*, 2021, **32**, 2106994.
33. D. Zhang, J. Cao, X. Zhang, N. Insin, S. Wang, J. Han, Y. Zhao, J. Qin and Y. Huang, *Adv. Funct. Mater.*, 2021, **31**, 2009412.
34. L. Ma, Y. Ying, S. Chen, Z. Huang, X. Li, H. Huang and C. Zhi, *Angew. Chem. Int. Ed.*, 2021, **60**, 3791-3798.
35. X. Li, N. Li, Z. Huang, Z. Chen, G. Liang, Q. Yang, M. Li, Y. Zhao, L. Ma, B. Dong, Q. Huang, J. Fan and C. Zhi, *Adv. Mater.*, 2021, **33**, e2006897.
36. X. Li, M. Li, Z. Huang, G. Liang, Z. Chen, Q. Yang, Q. Huang and C. Zhi, *Energy Environ. Sci.*, 2021, **14**, 407-413.
37. Y. Zou, T. Liu, Q. Du, Y. Li, H. Yi, X. Zhou, Z. Li, L. Gao, L. Zhang and X. Liang, *Nat. Commun.*, 2021, **12**, 170.
38. S. Li, Y. Liu, X. Zhao, Q. Shen, W. Zhao, Q. Tan, N. Zhang, P. Li, L. Jiao and X. Qu, *Adv. Mater.*, 2021, **33**, e2007480.
39. H. F. Li, Q. Yang, F. N. Mo, G. J. Liang, Z. X. Liu, Z. J. Tang, L. T. Ma, J. Liu, Z. C. Shi and C. Y. Zhi, *Energy Storage Mater.*, 2019, **19**, 94-101.
40. S. Li, Y. Liu, X. Zhao, K. Cui, Q. Shen, P. Li, X. Qu and L. Jiao, *Angew. Chem. Int. Ed.*, 2021, **60**, 20286-20293.
41. Y. Zeng, X. F. Lu, S. L. Zhang, D. Luan, S. Li and X. W. D. Lou, *Angew. Chem. Int. Ed.*, 2021, **60**, 22189-22194.
42. L. T. Ma, S. M. Chen, C. B. Long, X. L. Li, Y. W. Zhao, Z. X. Liu, Z. D. Huang, B. B. Dong, J. A. Zaprien and C. Y. Zhi, *Adv. Energy Mater.*, 2019, **9**, 1902446.